ACOUSTIC NEEDLES: 3D MICROFLUIDICS USING FOCUSED ULTRASOUND PASSING THROUGH HYDROPHOBIC MESHES

Yusuke Koroyasu[a,b], Thanh-Vinh Nguyen[c], Shun Sasaguri[a], Asier Marzo[d], Iñigo Ezcurdia[d], Yuuya Nagata[e], Takayuki Hoshi[f], Yoichi Ochiai[f,g,h], and Tatsuki Fushimi[g,h,1]

[a]School of Informatics, College of Media Arts, Science and Technology, University of Tsukuba, Tsukuba 305-8550, Japan
[b]Graduate School of Comprehensive Human Sciences, University of Tsukuba, Tsukuba 305-8550, Japan
[c]Sensing System Research Center, National Institute of Advanced Industrial Science and Technology (AIST), Tsukuba 305-8564, Japan
[d]Computer Science, Public University of Navarre, Pamplona 31006, Navarre, Spain
[e]Institute for Chemical Reaction Design and Discovery, Hokkaido University, Kita 21, Nishi 10, Kita-ku, Sapporo, Hokkaido 001-0021, Japan
[f]Pixie Dust Technologies, Inc., Tokyo 101-0061, Japan
[g]R&D Center for Digital Nature, University of Tsukuba, Tsukuba 305-8550, Japan
[h]Faculty of Library, Information and Media Science, University of Tsukuba, Tsukuba 305-8550, Japan
[1]To whom correspondence should be addressed. E-mail: tfushimi@slis.tsukuba.ac.jp

September 14, 2022

ABSTRACT

Current experiments in chemistry, biology, medicine, and engineering require the manipulation of multiple chemicals, samples, and specimens on a large scale. Therefore, automation techniques for manipulating microliter droplets are essential to improve the throughput, reproducibility, and sustainability of experiments. Digital microfluidic methods, such as EWOD (electrowetting-on-dielectric), electrostatics, and acoustophoretic platforms, offer excellent maneuverability and fast control for droplets. However, they are limited in terms of three-dimensional (3D) manipulation and droplet size. Here, we propose an acoustic needles platform, a 3D digital microfluidics system based on focused ultrasound waves (3D-MFUS) that pass through a hydrophobic mesh with droplets resting on it. A focused beam (acoustic needle), generated dynamically by a phased array, creates a stable trap through the mesh and attracts droplets to its focus. This needle can be steered to translate droplets on the surface; droplets can be manipulated simultaneously by generating multiple foci. Moreover, a liquid droplet can be detached from the surface and propelled into mid-air for up to 10.9 cm. This height is 27 and 2 times greater than that observed in the state-of-the-art methods in EWOD and photovoltaics, respectively. Droplets can be merged or split by pushing them against a hydrophobic knife. Additionally, both solid particles and liquid droplets can be manipulated using the same system. This platform would allow scientists and engineers to manipulate liquid droplets in a 3D circuit; moreover, it paves the way for developments in micro-robotics, additive manufacturing, and laboratory automation research.

***K*eywords** Microfluidics · Acoustic Radiation Force · Hydrophobic · Automation

1 Introduction

Microfluidics is becoming an ubiquitous approach in science and engineering [1, 2, 3, 4]. It is commonly used to automate and improve the throughput of experiments involving liquid droplets. Consequently, a wide range of digital microfluidic (DMF) platforms have been developed [5, 2, 3, 6, 1, 7, 8, 9, 10]; however, electrowetting on dielectric

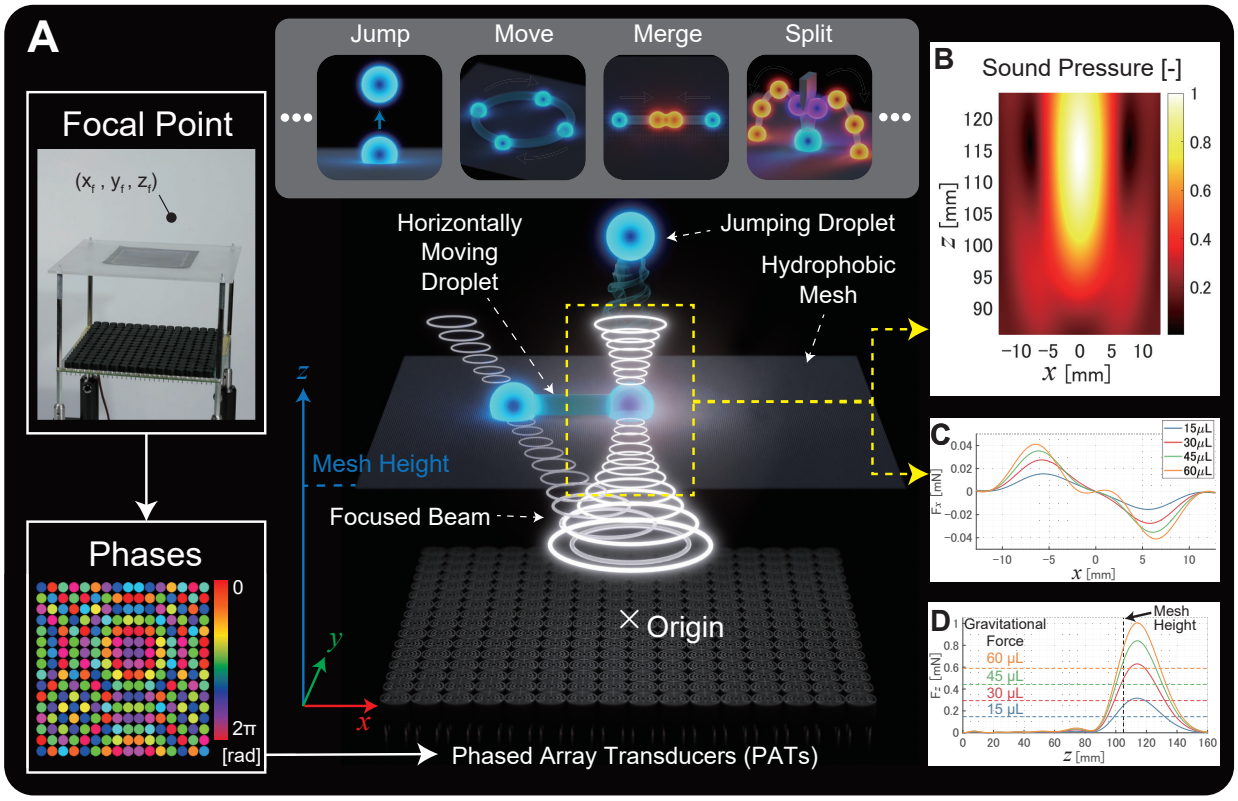

Figure 1: Schematic of the proposed system. (A) The target focal position is defined, and the necessary emission phases are calculated for each transducer of the PAT. Owing to the radiation force of the focused beam, the droplets jump, move, merge, or split above the hydrophobic mesh. (B) Simulated normalized sound pressure around the focal point (indicated by yellow in (A)) with focal point at $(x_f, y_f, z_f) = (0, 0, 115)$ mm. (C, D) Simulated acoustic radiation force for 15, 30, 45, and 60 µL droplets along the x and z directions with focal position at $(x_f, y_f, z_f) = (0, 0, 115)$ mm, with the mesh placed at $z = 105$ mm. The excitation voltage of the array in C is 10 V and that in D is 16 V for horizontal movements and jumping, respectively.

(EWOD) surfaces remains as the most common method. Although EWOD can manipulate a droplet over 2D surface grid, extending 2D microfluidics to 3D microfluidics is a necessary step forward [11, 12]. However, detaching droplets from a 2D surface is challenging. The achievable jump height is less than 5 mm with EWOD [13, 14, 11, 15]. Alternative 3D microfluidics methods have been proposed [16, 17, 18, 19] with jumping heights limited to 50 mm [12].

Containerless 3D microfluidics based on levitation techniques have also been studied. Acoustic levitation is preferred over other levitation techniques because it supports more materials and a microliter range of droplets [20]. In 2013, Foresti et al. [21] demonstrated the first horizontal mid-air merger. Despite its potential in 3D microfluidics; the use of standing waves is a necessity in current systems [22, 23, 24, 25], and this theoretically limits the droplet size to a quarter of the wavelength [26]. Given that the most frequently used frequency is 40 kHz ($\lambda = 8.5$ mm), the liquid-handling capability of a droplet is limited to ≈40 µL. Such a narrow droplet size range limits experimental applicability. Moreover, all droplets must be constantly levitated in acoustic levitation, which restricts the number of droplets that can be handled simultaneously. Finally, these systems can manipulate and merge the droplets but are unable to split them. Thus, a new approach that can handle a large number of liquid droplets of different sizes (>40 µL), manipulate them in 3D, and split them is needed.

Herein, we propose a 3D microfluidic device based on acoustic needles, as shown in Fig. 1A. An acoustic needle is created by a focused ultrasound beam that passes through an acoustically transparent mesh; liquid droplets are dispensed on top of the mesh with hydrophobic treatment (see Methods). The acoustic radiation forces (ARF) from the acoustic needles are applied using a phased array of transducers (PAT).

Owing to the hydrophobic treatment, the droplets rest on top of the mesh without permeating through; however, the acoustic waves can pass through the mesh. The PAT generates a focal point to focus ultrasonic power (Fig. 1B) slightly

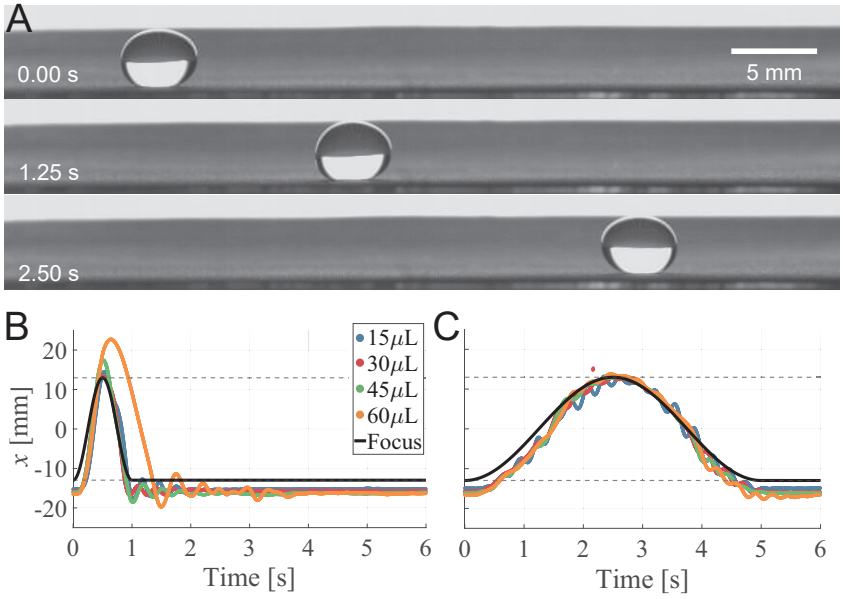

Figure 2: Horizontal manipulation of a droplet (applied voltage is 10 V). (A) Image series of a 45 µL droplet. The droplet was moved from left to right in the images for 25.6 mm (3.0λ) in 2.50 seconds. (B) Tracked position of droplets of different volumes along with the focal point when they move at $f = 1.0$ and (C) $f = 0.2$ Hz. See supplementary Movie S1.

above (10 mm) the target horizontal position of the droplet (see Methods). As is evident from Fig. 1C, this produces a stable and convergent ARF on the target along the horizontal directions (except for 60 µL droplets). The acoustic focal point position can be updated dynamically, and the droplet can be moved horizontally, if the focal point is in the vicinity of the droplet (approximately within a wavelength). A vertical ARF is also applied at the acoustic focal point (see Fig. 1D). The detachment of the droplet from the surface during the horizontal transportation can be prevented by lowering the acoustic pressure (Pa) applied to it (e.g., by lowering the voltage supplied to the PAT). However, when the droplet is required to jump above the surface, the acoustic pressure at the focal point is increased until the focus creates an ARF higher than the critical value ($> F_g + F_a$, where F_g and F_a are gravitational and adhesion forces, respectively). Because the droplets rest on the mesh without sticking to the surface, propulsion of a relatively large droplet can be induced using this approach, and multiple droplets can be manipulated with minimal force. We demonstrate that droplets greater than 40 µL can be handled using the proposed setup. In addition, we demonstrate that liquid droplets can be induced to jump to a height of up to 10.9 cm. The droplet can be split by placing a hydrophobic knife along the jump path. This 3D microfluidic platform can be used to automate pharmaceutical, biological, and chemical experiments both on Earth and under microgravity conditions. In addition, increased interactivity with microfluids would create new research avenues in interactive displays, micro-robotics, and additive manufacturing.

In the following sections, we describe the horizontal/vertical manipulation capabilities of the system and discuss droplet merging and splitting. In addition, we present proof-of-concept demonstrators (chemical reactions, surface cleaning, augmented reality application, and jumping into a cup) to highlight the potential of acoustic needles.

2 Results

2.1 Horizontal manipulation

The horizontal manipulation of a droplet on the hydrophobic mesh is achieved by steering the acoustic needles (i.e., controlling the position of the focal point). Using an acoustic focus is a counterintuitive choice considering the current trends in acoustic levitation. Conventional acoustic levitators use twin, bottle, or vortex traps to hold objects [27]. Owing to the acoustic contrast factor [28], rigid objects (including liquids [29, 21, 20]) in mid-air are expected to be pushed away from the focal point where the acoustic pressure is high. However, as shown in Fig. 1C, the focal point generates an attracting force, which is similar to that observed in underwater acoustics [30, 31]. Thus, the droplets can be manipulated on the mesh by simply controlling the position of the focal point and its power (Materials and

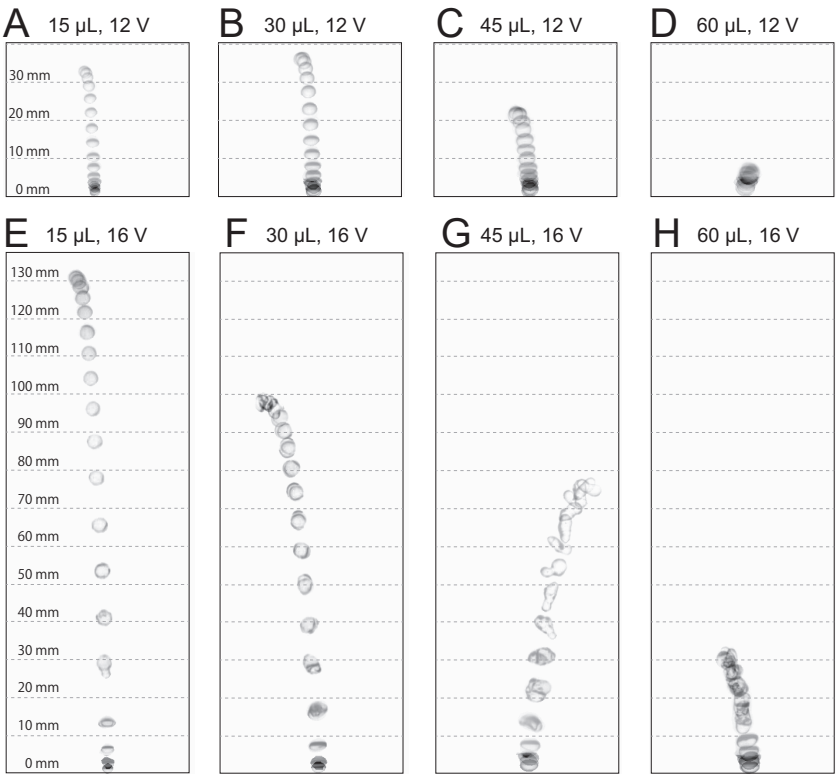

Figure 3: Jumping of a droplet from the mesh with (A, E) 15 µL, (B, F) 30 µL, (C, G) 45 µL, and (D, H) 60 µL. The applied voltage to the PAT was (A-D) 12 V and (E-H) 16 V. The sequence interval is 10 ms. The experiment was repeated five times. Notably, (D) only jumped once out of the five attempts because of its high mass and low supplied voltage. In (G-H), the droplet dispersed into multiple droplets 3 times out of 5 attempts. The video clip is provided in Movie S3.

Methods). The horizontal manipulation of a droplet is shown in Fig. 2 and Movie S1. The PAT phases were controlled such that $(x_f, y_f, z_f) = (-12.8\cos(2\pi ft), 0, 115)$ mm, where f is the frequency in Hz, with $0 \leq t \leq \frac{1}{f}$ and hold at $(x_f, y_f, z_f) = (-12.8, 0, 115)$ mm with $t > 1/f$.

Fig. 2A shows the time lapse of a moving droplet (45 µL), and Figs. 2B and C show the horizontal trajectory of the droplets moving at two frequencies ($f = 1.0, 0.2$ Hz) with four volumes (15, 30, 45, and 60 µL) and applied voltage of 10 V (see Methods). As shown in Fig. 2B and C, the droplets mostly follow the specified trajectory, except for 60 µL, which has a large mass and is difficult to move at a high speed. Some overshoot and underdamped oscillations are observed at $t = 1/2f$ and $1/f$ in Fig. 2B for all the droplets. Although underdamped oscillations are more prevalent during the movement in Fig. 2C than in B, the magnitude of the steady-state error is similar in both the cases. These trajectory errors are non-negligible; however, a closed-loop controller may be implemented to control the droplet more accurately. In the process of moving the droplets, generation of unexpected satellite droplets were not observed.

Solid spheres can also be manipulated using acoustic needles. Movie S2 shows the manipulation of nylon beads (MonotaRO Co., Ltd., density of $1140\,\mathrm{kg\,m^{-3}}$) with radii of 1.5, 2.0, and 2.5 mm. The ability to move both objects regardless of their properties (solids or liquids) is unique to acoustophoretics.

2.2 Jumping from the Mesh

The focused ultrasound beam applies a force along its traveling direction (Fig. 1D). When the ARF exceeds the critical value (i.e., ARF> sum of gravitational and adhesion forces, the voltage level at which the droplet detaches itself from the surface is provided in the supplementary material), the droplet detaches from the surface and jumps in mid-air. Fig. 3 shows the detachment process of droplets from the mesh. The droplet initially rests on top of the mesh ($(x, y, z) = (0, 0, 105)$ mm), and the focal point is aimed at $(x_f, y_f, z_f) = (0, 0, 115)$ mm for all the cases in Fig. 3.

We demonstrate the jumping of the droplet with 15, 30, 45, and $60\,\mu$L (see Methods for the experimental setup). The voltage applied to the transducers was 12 and 16 V. Sixty percent of the transducers were initially turned off to apply a lower amplitude and thus keep the droplet trapped. The detachment was then achieved by turning on all the transducers. Because there was some variability in projectile motion, the experiment was repeated five times. Here, the jumping height is defined as the difference between the centroid of the droplet at the peak height and the beginning of the jump. When the applied voltage was 12 V, the average jumping height was 30.7 (SD = 0.78), 33.2 (SD = 1.87), 15.8 (SD = 4.23), and 3.25 mm (SD = 0.75) for 15, 30, 45, and $60\,\mu$L, respectively (Fig. 3A-D). Notably, $60\,\mu$L droplet failed to detach once within five attempts, owing to high mass and low ARF generated.

When the applied voltage was increased to 16 V, the average jumping height increased to 108.8 (SD = 15.05), 78.0 (SD = 15.71), 59.7, 27.4 mm for 15, 30, 45, and $60\,\mu$L, respectively (Fig. 3E-H). The maximum average height of 108.8 mm represents 27, 7, and 2 times more than the jumping heights reported by the EWOD [14], pyroelectric [18], and photovoltaic [12] methods, respectively. The maximum recorded jumping height is 128.2 mm with $15\,\mu$L at 16 V. Large droplets can be detached as shown in Fig. 3G and H. However, the droplet splits into multiple droplets in the process; this occurred in 3 out of 5 attempts at 45 and $60\,\mu$L. The surface tension increases as the droplet radius exceeds the capillary length (2.3 mm in the case of water), and the droplets above this radius break easily into small droplets, owing to surface instability. Thus, it makes difficult for ARF to overcome gravity and surface tension without breaking the droplet. Further analysis is needed to make a large droplet jump without dispersion, which could be possible by applying a dynamic ease-in/ease-out in the amplitude of the focal point over time.

Although the observed motion of the droplets and numerical simulation results are generally consistent, some discrepancies exist. For example, even when the numerical simulation predicts that droplets will not jump, they jump in the experiment (see supplementary material). We believe that this discrepancy is because we assume the droplet to be spherical in the simulation, but the droplet is not perfectly spherical in reality because of the wetting caused by the mesh and the gravity. Therefore, the surface area impinged by the focal point is larger than that if the droplet is a perfect sphere, which increases the force applied to the droplet. Movie S4 tests this hypothesis and compares behavior of a solid sphere and droplet with the same volume. When the applied voltage is 12 V, all solid spheres with a radius of 1.5, 2.0, and 2.5 mm do not jump as predicted by the numerical simulation, while solids with a radius of 1.5, 2.0 and 2.5 mm jumped with 16 V, as the numerical simulation predicted (see supplementary material for details).

Moreover, while the focal point was kept stationary during the jump in this study, it could also be shifted while in mid-air, to match the droplet position. Potentially, the droplet trajectory could be changed in mid-air or a double jump can be performed. This can be used to increase the vertical travel distance, achieve free-space manipulations in microgravity environments, or generate displays in mid-air [32].

2.3 Merging multiple droplets

Various droplets can be manipulated simultaneously by generating multiple focal points. Here, we generate two focal points using the method developed by Andrade et al. [22] (half of the transducers were focused on droplet A, whereas the other half focused on droplet B). Simultaneous manipulation can also be achieved by generating multiple foci using optimization methods [33, 34, 35].

Fig. 4 shows the merging process of two droplets ($30\,\mu$L) at a supplied voltage of 25 V. The focal points were initially placed at $(x_f, y_f, z_f) = (\pm 6.39\left\{1+\cos(2\pi ft)\right\}, 0, kft+115)$ mm, where $f = 0.4$ Hz ($0 \leq t \leq 1.25$ s). If the two focal points are only translated horizontally (i.e., $k = 0$), the droplets jump and disperse as soon as they merge (Movie S5). Thus, the focal point was simultaneously shifted in the vertical direction to avoid jumping after coalescence. In Fig. 4, the value is set to $k = 20$. A suitable k value is different for each height and volume. If the gradient of the vertical shift is too high (e.g., when $k = 40$), then the droplets fail to merge. Similarly, in Fig. 2B and C, each droplet approaches the center ($x = 0$) along the specified trajectory with some underdamped oscillations. The droplets then merged near the center at approximately 0.84 s. The oscillations generated by the merging decay, and the droplet stabilizes at the center.

While acoustic levitation in a standing wave configuration can achieve merging in mid-air [21, 22, 23]; it cannot continue to levitate the merged droplets if the combined size is larger than quarter wavelength limit. Because the droplet rests on the mesh, it can be processed for further experiments and analysis.

2.4 Splitting

Here, we demonstrate the splitting of a droplet. A hydrophobically treated knife was placed vertically 5 mm above the mesh and the droplet ($45\,\mu$L with 12 V) was catapulted against the knife, as shown in Fig. 5A. The experimental process was the same as that used in the jump experiment. The knife cuts the droplet in half at approximately 70 ms, and the

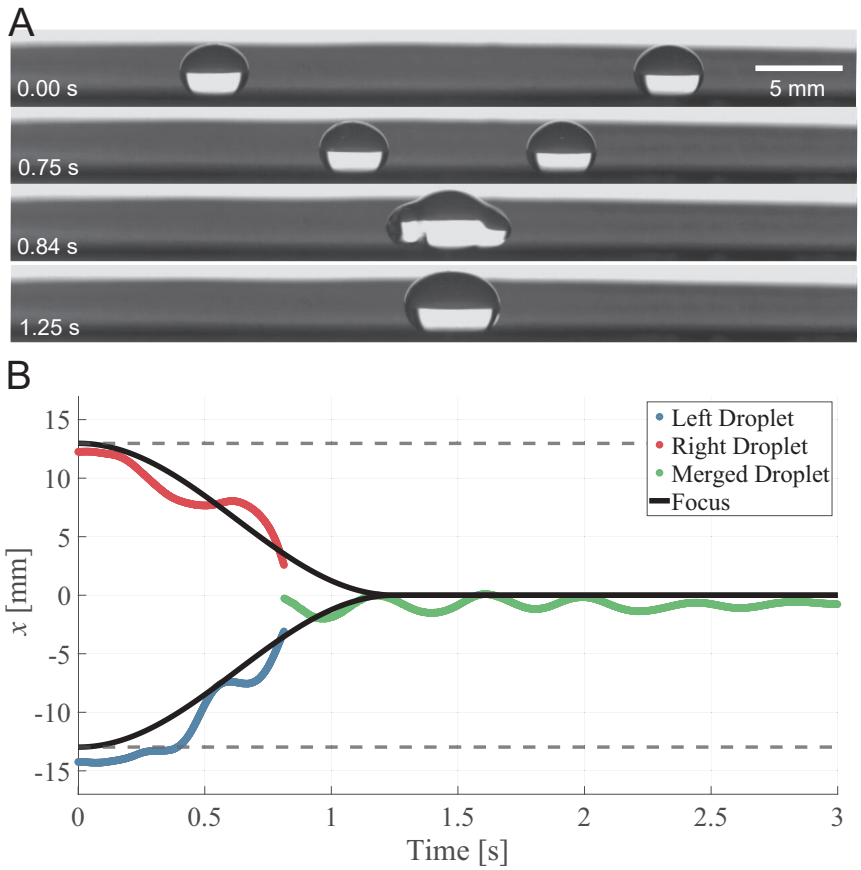

Figure 4: Merging two droplets with a supplied voltage of 25 V. (A) Two droplets were placed on the mesh at $(x, y, z) = (\pm 12.8, 0, 105)$ mm at $t = 0.0$ s, moved to the center, and merged at $t = 0.84$ s; eventually, the merged droplet becomes stable. (B) Experimental results for the horizontal position of the two droplets when $k = 20$, along with the foci.

droplet continues to travel vertically and land on the mesh after free-fall. Fifteen and 30 µL droplets could also be split (Movie S6). Whether the droplets can be successfully split is determined by the Weber number and the position where the droplet hits the knife [36]. Further studies are necessary to accurately split the droplets in the desired proportions.

2.5 Proof of Concept Demonstration

In the following section, we demonstrate four proof-of-concepts (PoCs) that highlight the potential of acoustic needles in relevant fields.

2.5.1 Chemical Reaction

In Fig. 5B and Movie S7, we demonstrate the chemical reaction between droplets of rice vinegar (30 µL of acetic acid (4.2 vol%) in water) and bromothymol blue (BTB) solution (30 µL of BTB (0.04 wt%) dissolved in water). Because the applied acoustic force is independent of the material properties of the target, any droplet can be moved using acoustic needles. System applicability is limited only when the liquid is not repelled by the mesh and sticks or permeates it. We tested various chemicals that could be used in our current setup, and currently it is limited to dimethylsulfoxide or aqueous solutions (see supplementary material). Other chemicals such as tetrahydrofuran and toluene permeate through the mesh. Acetonitrile and *N*,*N*-dimethylformamide (DMF) do not permeate but stick to the surface. This limitation is bounded to our current hydrophobic mesh; however, Pan et al. [37] demonstrated a superomniphobic mesh coating method that can repel a wider range of chemicals, including DMF and toluene. The mesh used by Pan et al. was less dense than that used in our study. Thus, employing a superomniphobic mesh in acoustic needles would yield a high-performance microfluidic platform in terms of the acoustic force that passes through the mesh and the supported compounds.

2.5.2 Surface Cleaning

We demonstrate the cleaning of the substrate surface by manipulating a water droplet (30 µL, 11 V) in Fig. 5C and Movie S8. The droplet was moved in a circular trajectory of radius 10 mm to collect a solid object (glass bead, TOHO Co., Ltd., density of 2500 kg m^{-3}, outer diameter is 2.0 mm, height is 1.4 mm, inside hole diameter is 0.9 mm) in the trajectory (0.57 s). After collection, the droplet and bead returned to the initial position. This operation is needed in

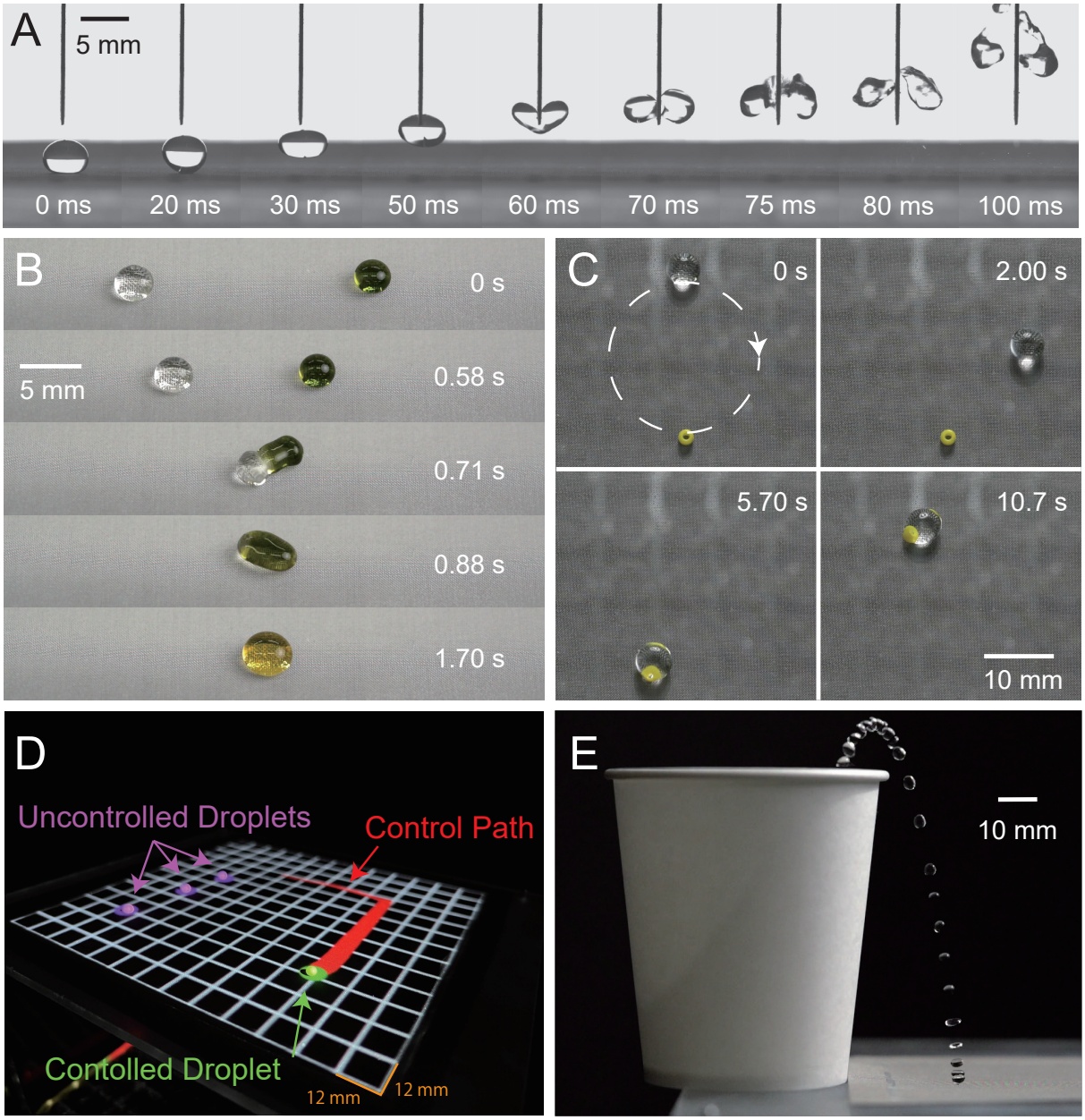

Figure 5: Potential applications of acoustic needles. (A) Splitting of a liquid droplet (45 µL) by catapulting it into a hydrophobic knife placed 5 mm above the mesh. (B) Chemical reaction between rice vinegar and BTB solution (both 30 µL), the two droplets merge and change the color of BTB to yellow, indicating acidity. (C) Residues can be cleaned up using a water droplet. (D) Demonstration of augmented reality with images projected from a projector fixed above the mesh, 15 µL milk droplets were used to improve visibility. Selective manipulation of the droplets is possible, non-manipulated droplets remain stationary. (E) Droplet (15 µL, 17 V) jumping into a paper cup (height 80 mm).

experimental automation to clean residues between trials. These beads are difficult to manipulate using acoustophoretic forces because of their large mass; however, they can be easily transported by carrying them inside a water droplet.

2.5.3 AR application

In Fig. 5D and Movie S9, we demonstrate an augmented reality (AR) application that combines acoustic needles and projection mapping. Users draw a path on a GUI and the PAT plays back the trajectory of the droplet. Simultaneously, information regarding the path and position of the droplet is projected onto the mesh. This could further improve human interaction with the systems when the experiments are not fully automatic and require human intervention. This system was created using TouchDesigner (Derivative Inc.).

2.5.4 Jumping into a cup

The ability to propel droplets above 10 cm allows achieving a wider range of tasks. For example, Fig. 5E and Movie S10 show a water droplet (15 µL, 17 V) which is placed on $(x, y, z) = (-20, 0, 105)$ mm jumping diagonally into a cup (height = 80 mm). Applications in the food industry, additive manufacturing, or throwing droplets to other processor/analyzer/waste bins for experimental automation can be realized with such three-dimensional manipulation capabilities.

3 Conclusion

We proposed acoustic needles, a three-dimensional microfluidics platform with focused ultrasound passing through a hydrophobic mesh that holds droplets on the top. We demonstrated the fundamental horizontal/vertical manipulation capabilities of the proposed device and operations such as merging and splitting. The maximum average jumping height achieved by the acoustic needle is up to 27 times higher than that of the conventional DMF. Moreover, we presented four proof-of-concepts that highlight the potential applicability of the proposed device in multiple fields. Acoustic needles could create new research avenues in microfluidics owing to their superior three-dimensional capability.

4 Material and Method

Here we describe the experimental setup and numerical simulation.

4.1 Phased Array Transducer

4.1.1 Hardware

A 16×16 transducer array (256 transducers) developed based on Morales et al. [38] instructions was used throughout the experiments. The transducers used were Murata MA40S4S (40 kHz). The array was controlled via serial communication (USB FTDI cable with baud rate = 230400) with MOFSETs (MIC4127 SOIC8) and an FPGA board (ALTERA Core Board CoreEP4CE6). Full details regarding the hardware (SonicSurface) are available at the Instructables by UpnaLab[1]. The voltage applied to the PAT was controlled by adjusting the external power supply (RS PRO bench power supply, IPS-303A, 90W).

4.1.2 Acoustic Hologram

To manipulate the target objects dynamically, an acoustic hologram was generated to create a focal point at the target position $\boldsymbol{x_t}$:

$$\phi_t = -\frac{2\pi f_0}{c_0}\left[d(\boldsymbol{x_f}, \boldsymbol{x_t}) - d(0, \boldsymbol{x_f})\right], \tag{1}$$

where $f_0 = 40$ kHz and $c_0 = 341\,\mathrm{ms}^{-1}$ are the acoustic frequency and speed of sound in the air, respectively. d is the Euclidean distance between two points. $\boldsymbol{x_f} = (x_f, y_f, z_f)$ and $\boldsymbol{x_t} = (x_t, y_t, z_t)$ denote the focal position and transducer positions, respectively.

4.2 Hydrophobic Mesh

A mesh (Q-ho Metal Works, part number E9122, stainless steel SUS316, plain weave, mesh count 150) was hydrophobically treated by spraying with Ultra-Ever Dry (UltraTech International Inc.). First, a bottom coat was applied and dried.

[1] https://www.instructables.com/SonicSurface-Phased-array-for-Levitation-Mid-air-T/

When the bottom coating was sufficiently dry, the top coating was applied and dried again. Advancing and receding contact angle were $155.7^\circ \pm 1.5^\circ$ and $138.4^\circ \pm 4.4^\circ$, respectively (i.e., contact angle hysteresis was $17.3^\circ \pm 5.1^\circ$). The mesh was mounted on top of a 4 mm thick acrylic plate (180×180 mm) with a square hole (80×80 mm) cut open in the center. For Fig. 5D, the same hydrophobic coating was used; however, a high-rigidity tungsten mesh (Clever Co., Ltd., plain weave, mesh count 150) was used to allow a large working area and minimize reflections from the surface for visibility.

4.3 Liquid and its dispense

Deionized water (KOGA Chemical Mfg Co., Ltd.) was used throughout the study, unless otherwise stated. Water was dispensed using a syringe pump (Chemyx Fusion 101) in Fig. 2, 3, 4, and 5A. For Figs. 5B, C, and E, an electronic pipette (A&D Company, MPA-200) was used to dispense the liquid.

4.4 Recording Devices

The movement of the droplet was captured using a high-speed camera (Photron INFINICAM UC-1) with a Nikon F to C Mount Adaptor (Kenko Tokina) and a single-focus lens (Tamron SP AF180mm F/3.5Di). The camera was connected to a PC using USB C cable and controlled using Python 3.7. In Figs. 2, 4, and 5A, the frame rate and image resolutions were fixed at 1000 fps and 1246×1024 pixels, respectively. The frame rate and image resolution were 2000 fps and 512×1246 pixel, respectively in Fig. 3. The camera was triggered to start recording when commands were sent to the PAT. To capture the images presented in Fig. 5B, C, and E, a Sony $\alpha 7$ (FE 2.8/90 MACRO lens) was used. Fig. 5D was captured using iPhone 13 Pro.

4.5 Image Processing and Analysis

Image processing was performed using MATLAB R2020a. Lens calibration was performed using a checkerbox with MATLAB Computer Vision Toolbox (ver. 9.2). The pixel-to-mm conversion rate was obtained by placing an object of a known size (i.e., ruler) at the $x - z$ plane ($y = 0$). The droplet position was analyzed by subtracting the droplet from the background image. The subtracted portion was then passed onto $regionprops$ function in the MATLAB Image Processing Toolbox (ver. 11.1) to identify the droplet centroid. The sequence photographs (Fig. 3, 5E) were also generated by overlaying the background-subtracted images. The code to replicate analysis is available in the data availability section.

4.6 Numerical Simulation

The numerical simulations in this study were performed using MATLAB R2020a. Codes to fully replicate the simulation results are presented in the data availability section.

4.6.1 Acoustic Pressure Field

The acoustic pressure field shown in Fig. 1B was calculated based on the Huygens' principle as follows:

$$p_{in}(x, x_t, \phi_t) = \sum_{t=1}^{T} \frac{P_0}{d(\boldsymbol{x}, \boldsymbol{x_t})} D(\eta) e^{j(kd(\boldsymbol{x}, \boldsymbol{x_t}) + \phi_t)}, \tag{2}$$

where p_{in} is the sound pressure and transducer number (T) is 256. $D(\eta) = \frac{2J_1(kr\sin\eta)}{kr\sin\eta}$ denotes the far-field directivity function of the piston source. η is the angle between the normal of the transducer and position $\boldsymbol{x}$. $k = \frac{2\pi f_0}{c_0}$ is the wavenumber. P_0 denotes the transducer power. We report $P_v = 0.221\,\mathrm{Pa\,V^{-1}}$ at 1 m for Murata MA40S4S; P_0 is evaluated by multiplying the applied voltage (A_v): $P_0 = A_v P_v$.

4.6.2 Acoustic Radiation Force

The acoustic radiation force (ARF) is typically calculated using the method proposed by Gor'kov [39]. However, because the PAT contains strong travelling wave components and uses droplet sizes larger than the Rayleigh limit (i.e.,

r>0.1λ), we used the method developed by Andersson & Ahrens to calculate the ARF [40, 41]:

$$F_x = \frac{1}{8\rho_0 c_0^2 k^2} \mathrm{Re}\left\{ \sum_{n=0}^{\infty} \sum_{m=-n}^{n} \Psi_n A_{nm} \left(S_{n,m} S^*_{n+1,m+1} - S_{n,-m} S^*_{n_1,-m-1} \right) \right\} \tag{3}$$

$$F_y = \frac{1}{8\rho_0 c_0^2 k^2} \mathrm{Im}\left\{ \sum_{n=0}^{\infty} \sum_{m=-n}^{n} \Psi_n A_{nm} \left(S_{n,m} S^*_{n+1,m+1} + S_{n,-m} S^*_{n_1,-m-1} \right) \right\} \tag{4}$$

$$F_z = \frac{1}{8\rho_0 c_0^2 k^2} \mathrm{Re}\left\{ \sum_{n=0}^{\infty} \sum_{m=-n}^{n} \Psi_n B_{nm} \left(S_{n,m} S^*_{n+1,m} \right) \right\} \tag{5}$$

where $\Psi = 2i(c_n + c^*_{n+1} + 2c_n c^*_{n+1})$, $A_{nm} = \sqrt{\frac{(n+m+1)(n+m+2)}{(2n+1)(2n+3)}}$, and $B_{nm} = -2\sqrt{\frac{(n+m+1)(n-m+1)}{(2n+1)(2n+3)}}$. Here, we assume that the target is solid (i.e., the liquid is rigid in comparison to air) and that it is perfectly spherical.

$$c_n = -\frac{j_n(ka) j'_n(k_p a) - Z j'_n(ka) jn(k_p a)}{h_n(ka) j'_n(k_p a) - Z h'_n(ka) j_n(k_p a)} \tag{6}$$

where $Z = \frac{\rho_p c_p}{\rho_0 c_0}$ is the relative impedance, with subscript 0 indicating the medium, and p indicates the sphere. The asterisk * indicates a complex-conjugated element. For a water droplet, the density and speed of sound are assumed to be $1000\,\mathrm{kg\ m^{-3}}$ and $1480\,\mathrm{m\ s^{-1}}$, respectively. j_n and h_n are the spherical Bessel and Hankel functions of the first kind, respectively. ' indicates the derivative of each function. This method was independently verified and expanded to include the piston source model by Zehnter et al. [42]:

$$S_{n,m} = \sum_t 4\pi P_0 e^{(j\phi_t)} D(\eta) ikh_n(kr^t) Y^*_{nm}(\theta^t, \phi^t). \tag{7}$$

Y_{nm} is the spherical harmonics function, which was implemented using the code developed by Javier Montalt Tordera[2]. (r^t, θ^t, ϕ^t) are in spherical coordinates and calculated from the center of the levitated sphere to the transducer. The center of the sphere was assumed to be the mesh height plus the radius of the droplet (assuming a perfect sphere). Equations 3 to 5 were evaluated until the relative tolerance was less than 1×10^{-5}. We verified the validity of the numerical simulation above, and are available in the supplementary material.

Data Availability

The data that support the findings of this study are available within this paper, its supplementary material, and in Zenodo at http://doi.org/[doi].

Acknowledgement

This work was supported by JSPS KAKENHI Grant Number JP21K14103. We would like to thank Mr. Atsushi Shinoda for his assistance with experimental apparatus manufacturing. We also acknowledge the assistance of Mr. Kenta Yamamoto on photography. We would like to thank Editage [http://www.editage.com] for editing and reviewing this manuscript for English language.

Author Contributions

Y.K., N.T., Y.O., and T.F. designed the research methodology. Y.K., N.T., S.S., A.M., and I.E. contributed to the design and manufacture of the experimental apparatus. Y.K. and T.F. contributed to the design of the experiments. Y.K., S.S., and Y.N. collected the experimental data. T.F. developed and conducted the numerical simulations. Y.K. performed image processing, and Y.K., Y.N., T.H., Y.O., and T.F. analyzed and discussed the results. All authors contributed to drafting the manuscript.

Conflict of Interest

A patent application (JP2022-122138) was filed in relation to this publication.

[2]https://github.com/jmontalt/harmonicY

References

[1] R. B. Fair. Digital microfluidics: is a true lab-on-a-chip possible? *Microfluidics and Nanofluidics*, 3(3):245–281, apr 2007.

[2] Sidra Waheed, Joan M. Cabot, Niall P. Macdonald, Trevor Lewis, Rosanne M. Guijt, Brett Paull, and Michael C. Breadmore. 3D printed microfluidic devices: Enablers and barriers. *Lab on a Chip*, 16(11):1993–2013, 2016.

[3] Yi Zhang and Nam Trung Nguyen. Magnetic digital microfluidics - a review. *Lab on a Chip*, 17(6):994–1008, 2017.

[4] Udayan Umapathi, Patrick Shin, Ken Nakagaki, Daniel Leithinger, and Hiroshi Ishii. Programmable Droplets for Interaction. In *Extended Abstracts of the 2018 CHI Conference on Human Factors in Computing Systems*, pages 1–1, New York, NY, USA, apr 2018. ACM.

[5] Thomas Franke, Adam R Abate, David A Weitz, and Achim Wixforth. Surface acoustic wave (saw) directed droplet flow in microfluidics for pdms devices. *Lab on a Chip*, 9(18):2625–2627, 2009.

[6] Xin Tang, Pingan Zhu, Ye Tian, Xuechang Zhou, Tiantian Kong, and Liqiu Wang. Mechano-regulated surface for manipulating liquid droplets. *Nature Communications*, 8:1–10, 2017.

[7] Yuankai Jin, Wanghuai Xu, Huanhuan Zhang, Ruirui Li, Jing Sun, Siyan Yang, Minjie Liu, Haiyang Mao, and Zuankai Wang. Electrostatic tweezer for droplet manipulation. *Proceedings of the National Academy of Sciences*, 119(2), 2022.

[8] Chao Yang, Yongfeng Ning, Xiaoyong Ku, Guisheng Zhuang, and Gang Li. Automatic magnetic manipulation of droplets on an open surface using a superhydrophobic electromagnet needle. *Sensors and Actuators, B: Chemical*, 257:409–418, 2018.

[9] Qiangqiang Sun, Dehui Wang, Yanan Li, Jiahui Zhang, Shuji Ye, Jiaxi Cui, Longquan Chen, Zuankai Wang, Hans Jürgen Butt, Doris Vollmer, and Xu Deng. Surface charge printing for programmed droplet transport. *Nature Materials*, 18(9):936–941, 2019.

[10] Sung Kwon Cho, Hyejin Moon, and Chang-Jin Kim. Creating, transporting, cutting, and merging liquid droplets by electrowetting-based actuation for digital microfluidic circuits. *Journal of Microelectromechanical Systems*, 12(1):70–80, feb 2003.

[11] Jeong Byung Chae, Seung Jun Lee, Jinseung Yang, and Sang Kug Chung. 3D electrowetting-on-dielectric actuation. *Sensors and Actuators, A: Physical*, 234:331–338, 2015.

[12] Yuhang Mi, Xiaohu Liu, Zuoxuan Gao, Mengtong Wang, Lihong Shi, Xiong Zhang, Kaifang Gao, Euphrem Rwagasore Mugisha, and Wenbo Yan. 3D Photovoltaic Router of Water Microdroplets Aiming at Free-Space Microfluidic Transportation. *ACS Applied Materials & Interfaces*, 13(37):45018–45032, sep 2021.

[13] Seung Jun Lee, Sanghyun Lee, and Kwan Hyoung Kang. Droplet jumping by electrowetting and its application to the three-dimensional digital microfluidics. *Applied Physics Letters*, 100(8):081604, 2012.

[14] Seung Jun Lee, Jiwoo Hong, Kwan Hyoung Kang, In Seok Kang, and Sang Joon Lee. Electrowetting-induced droplet detachment from hydrophobic surfaces. *Langmuir*, 30(7):1805–1811, 2014.

[15] Zhantao Wang, Dirk van den Ende, Arjen Pit, Rudy Lagraauw, Daniël Wijnperlé, and Frieder Mugele. Jumping drops on hydrophobic surfaces, controlling energy transfer by timed electric actuation. *Soft Matter*, 13(28):4856–4863, 2017.

[16] Koji Takeda, Akira Nakajima, Kazuhito Hashimoto, and Toshiya Watanabe. Jump of water droplet from a super-hydrophobic film by vertical electric field. *Surface science*, 519(1-2):L589–L592, 2002.

[17] B. Traipattanakul, C.Y. Tso, and Christopher Y.H. Chao. Study of jumping water droplets on superhydrophobic surfaces with electric fields. *International Journal of Heat and Mass Transfer*, 115:672–681, dec 2017.

[18] Weishan Yan, Chaopeng Zhao, Wenyao Luo, Wangyang Zhang, Xi Li, and Duo Liu. Optically Guided Pyroelectric Manipulation of Water Droplet on a Superhydrophobic Surface. *ACS Applied Materials and Interfaces*, 13(19):23181–23190, 2021.

[19] Ning Li, Lei Wu, Cunlong Yu, Haoyu Dai, Ting Wang, Zhichao Dong, and Lei Jiang. Ballistic Jumping Drops on Superhydrophobic Surfaces via Electrostatic Manipulation. *Advanced Materials*, 30(8):1703838, feb 2018.

[20] Marco A. B. Andrade, Nicolás Pérez, and Julio C. Adamowski. Review of Progress in Acoustic Levitation. *Brazilian Journal of Physics*, 48(2):190–213, apr 2018.

[21] D. Foresti, M. Nabavi, M. Klingauf, A. Ferrari, and D. Poulikakos. Acoustophoretic contactless transport and handling of matter in air. *Proceedings of the National Academy of Sciences*, 110(31):12549–12554, 2013.

[22] Marco A. B. Andrade, Thales S. A. Camargo, and Asier Marzo. Automatic contactless injection, transportation, merging, and ejection of droplets with a multifocal point acoustic levitator. *Review of Scientific Instruments*, 89(12):125105, 2018.

[23] Ayumu Watanabe, Koji Hasegawa, and Yutaka Abe. Contactless Fluid Manipulation in Air: Droplet Coalescence and Active Mixing by Acoustic Levitation. *Scientific Reports*, 8(1):10221, dec 2018.

[24] Stephen J Brotton and Ralf I Kaiser. Controlled chemistry via contactless manipulation and merging of droplets in an acoustic levitator. *Analytical Chemistry*, 92(12):8371–8377, 2020.

[25] Teruhiko Matsubara and Kenjiro Takemura. Containerless Bioorganic Reactions in a Floating Droplet by Levitation Technique Using an Ultrasonic Wave. *Advanced Science*, 8(3):1–5, 2021.

[26] R. R. Whymark. Acoustic field positioning for containerless processing. *Ultrasonics*, 13(6):251–261, nov 1975.

[27] Asier Marzo, Sue Ann Seah, Bruce W. Drinkwater, Deepak Ranjan Sahoo, Benjamin Long, and Sriram Subramanian. Holographic acoustic elements for manipulation of levitated objects. *Nature Communications*, 6(May):8661, oct 2015.

[28] Henrik Bruus. Acoustofluidics 7: The acoustic radiation force on small particles. *Lab on a Chip*, 12(6):1014–1021, 2012.

[29] Asier Marzo, Adrian Barnes, and Bruce W. Drinkwater. TinyLev: A multi-emitter single-axis acoustic levitator. *Review of Scientific Instruments*, 88(8):085105, aug 2017.

[30] Kai Melde, Andrew G. Mark, Tian Qiu, and Peer Fischer. Holograms for acoustics. *Nature*, 537(7621):518–522, 2016.

[31] Luke Cox, Kai Melde, Anthony Croxford, Peer Fischer, and Bruce W Drinkwater. Acoustic Hologram Enhanced Phased Arrays for Ultrasonic Particle Manipulation. *Phys. Rev. Applied*, 12(6):64055, dec 2019.

[32] Tatsuki Fushimi, Asier Marzo, Bruce W Drinkwater, and Thomas L Hill. Acoustophoretic volumetric displays using a fast-moving levitated particle. *Applied Physics Letters*, 115(6):064101, 2019.

[33] Benjamin Long, Sue Ann Seah, Tom Carter, and Sriram Subramanian. Rendering volumetric haptic shapes in mid-air using ultrasound. *ACM Transactions on Graphics (TOG)*, 33(6):1–10, 2014.

[34] Asier Marzo and Bruce W. Drinkwater. Holographic acoustic tweezers. *Proceedings of the National Academy of Sciences*, 116(1):84–89, 2018.

[35] Tatsuki Fushimi, Kenta Yamamoto, and Yoichi Ochiai. Acoustic hologram optimisation using automatic differentiation. *Scientific Reports*, 11(1):12678, jun 2021.

[36] Thanh-Vinh Nguyen, Hironao Okada, Yuki Okamoto, Yusuke Takei, Atsushi Takei, and Masaaki Ichiki. Direct measurement of impacting force between a droplet and a superhydrophobic blade. In *2021 IEEE 34th International Conference on Micro Electro Mechanical Systems (MEMS)*, pages 771–774, 2021.

[37] Shuaijun Pan, Arun K Kota, Joseph M Mabry, and Anish Tuteja. Superomniphobic surfaces for effective chemical shielding. *Journal of the American Chemical Society*, 135(2):578–581, 2013.

[38] Rafael Morales, Iñigo Ezcurdia, Josu Irisarri, Marco AB Andrade, and Asier Marzo. Generating airborne ultrasonic amplitude patterns using an open hardware phased array. *Applied Sciences*, 11(7):2981, 2021.

[39] L. P. Gor'kov. On the Forces Acting on a Small Particle in an Acoustical Field in an Ideal Fluid. *Soviet Physics Doklady*, 6:773, 1962.

[40] Carl Andersson and Jens Ahrens. Acoustic levitation from superposition of spherical harmonics expansions of elementary sources: Analysis of dependency on wavenumber and order. In *2019 IEEE International Ultrasonics Symposium (IUS)*, pages 920–923. IEEE, 2019.

[41] Carl Andersson. Acoustic levitation of multi-wavelength spherical bodies using transducer arrays of non-specialized geometries. *The Journal of the Acoustical Society of America*, 151(5):2999–3006, may 2022.

[42] Sebastian Zehnter, Marco A. B. Andrade, and Christoph Ament. Acoustic levitation of a Mie sphere using a 2D transducer array. *Journal of Applied Physics*, 129(13):134901, apr 2021.